Supporting Information for

Nanoscale Fluid Vortices and Nonlinear Electroosmotic Flow Drive Ion Current Rectification in the Presence of Concentration Gradients

Jake Rabinowitz[1], *Martin A. Edwards*[3], *Elizabeth Whittier*[1], *Krishna Jayant*[1,2], *Kenneth Shepard*[1]

1 Bioelectronic Systems Laboratory, Department of Electrical Engineering, Columbia University, NY 10027, USA

2 Department of Biological Sciences, Columbia University, NY 10027, USA

3 Department of Chemistry, University of Utah, UT 84112, USA

Table of Contents

1. Simulation theory and verification

1a. Finite element theory

We employ a finite element model to solve the coupled Poisson-Nernst Planck-Navier Stokes (P-NP-NS) equations and gain insight into the physical processes occurring at the pipette tip. A two-dimensional axisymmetric model self-consistently solves the P-NP-NS equations, determining steady-state voltage, concentration, velocity, and pressure distributions with respect to radial and axial coordinates. The continuum approach is deemed appropriate based on a small experimental Knudsen number (Kn < 0.05), where the Knudsen number is a dimensionless ratio of molecular mean free path (~2.5 Å in water) to minimum geometric length scale (pipette radius > 5 nm). Continuum approaches remain valid until Kn approaches unity.

The Poisson equation governs electrostatics according to the space charge model for a binary monovalent electrolyte,

$$\nabla^2 V = -\frac{F}{\varepsilon}(c_+ - c_-) \quad \text{(S1)}$$

where V is voltage, F is the Faraday constant, ε is electrolyte permittivity, c_+ is cation (K^+) concentration, and c_- is anion (Cl^-) concentration.

The Nernst-Planck equation governs ion transport, respectively accounting for diffusive, electrophoretic, and convective flux as

$$\vec{N}_i = -D_i \nabla c_i + \frac{z_i F}{RT} D_i c_i \nabla V - c_i \vec{u} \quad \text{(S2)}$$

where $\vec{N}_i$ is molar flux of the ionic species i, D_i is diffusion coefficient, c_i is ion concentration, z_i is ion valence number, R is the universal gas constant, T is temperature, and $\vec{u}$ is fluid velocity.

The Navier-Stokes equation governs fluid flow, including a source term for EOF and neglecting the inertial term based on flow in the low-Reynolds number regime (Re << 1),

$$-\nabla P + \eta \nabla^2 \vec{u} + F(c_+ - c_-)\nabla V = 0 \quad \text{(S3)}$$

where P is pressure and η is fluid viscosity.

Included in **Figure S1** is the finite element geometry and imposed boundary conditions. Atop the pipette, experimental c_{in}, V, and P are applied, where P accounts for the small hydrostatic pressure ($P = \rho gh$) from the solution column above the pipette tip ($h \approx 5$ cm). At the spherical external solution boundary, experimental c_{ex}, $V = 0$, and $P = 0$ are imposed. All other boundaries are glass pipette walls, where constant surface charge (σ), no flux ($N_i = 0$), and no slip ($u = 0$) conditions are imposed. Any possible conduction through the wall of the pipette (due to glass hydration or porosity) is omitted, with resulting assumptions of ideally capacitive glass and only DC signals.

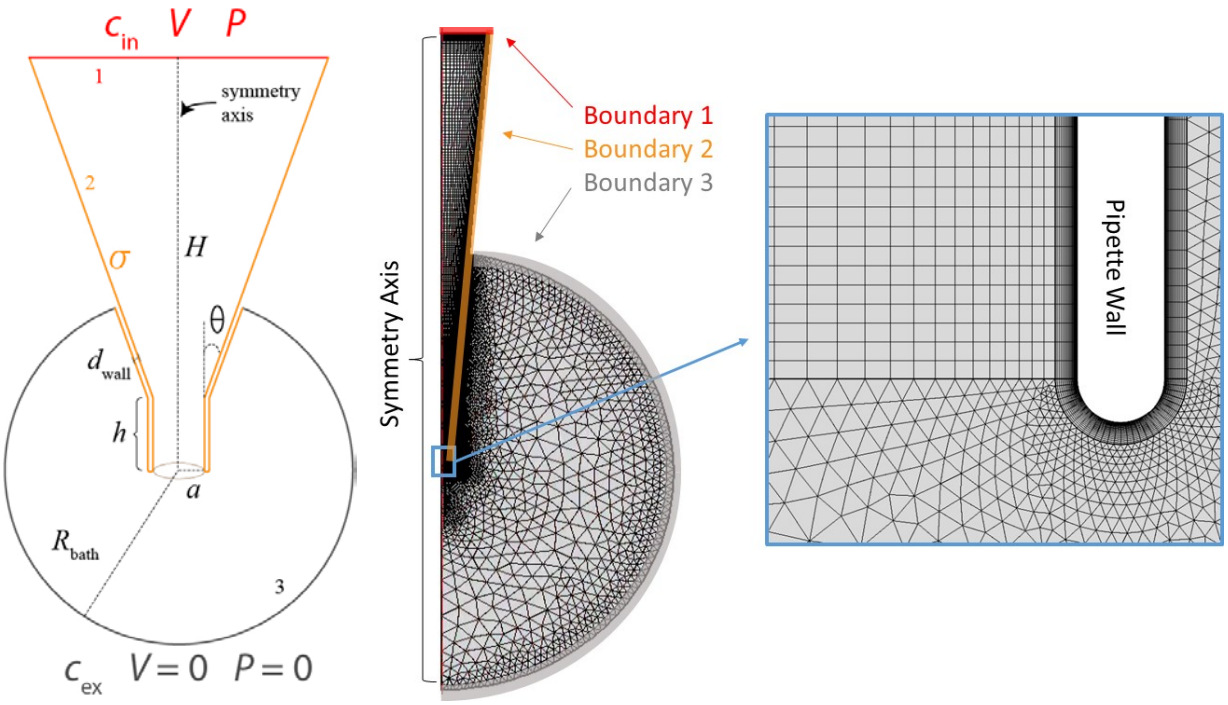

Figure S1. (Left) Schematic of finite element system employed in COMSOL, including boundaries and relevant geometric parameters. (Middle) Coarse view of axisymmetric finite element model, depicting boundaries and mesh. (Right) Expanded view of meshing and geometry at nanopipette tip.

Included in **Tables S1-S3** is a summary of boundary conditions for **Equations S1-S3** (**Table S1**), a list of the numerical parameters employed in simulations (**Table S2**), and a list of physical parameters for the experimental system (**Table S3**).

Boundary	Poisson	Nernst-Planck	Navier-Stokes
Internal Solution (1)	Applied Voltage $V = V$	Pipette Concentration $c = c_{in}$	Hydrostatic Pressure $P = 0.49\ kPa$
Pipette Walls (2)	Surface Charge $n \bullet \varepsilon \nabla V = \sigma$	No Flux $n \bullet \vec{N}_i = 0$	No-slip $\vec{u} = 0$
External Solution (3)	Ground $V = 0$	Bath Concentration $c = c_{ex}$	Atmospheric Pressure $P = 0$

Table S1. Boundary conditions imposed in the finite element simulation.

Parameter	Value (Figures 1-5)	Value (Figures 6-7)
a	12 nm	15 nm
σ	-8 mC/m^2	-12 mC/m^2
R_{bath}	0.25 μm	0.5 μm
H	0.5 μm	1.0 μm
h	50 nm	110 nm
θ	5^o	5^o
d_{wall}	2 nm	2 nm

Table S2. Theoretical pipette parameters, fit to experimental data. Above listed values and relevant boundary conditions compose the simulations employed for all results presented in the Main Text.

Parameter	Description	Value
D_{K+}	Diffusion Coefficient, K^+	1.957*10^{-9} m^2/s [1]
D_{Cl-}	Diffusion Coefficient, Cl^-	2.032*10^{-9} m^2/s [1]
ε_{H2O}	Electrolyte Permittivity	78.5
η	Electrolyte Viscosity	9.6*10^{-4} Pa*s [2]
ρ	Electrolyte Density	999 kg/m^3 [2]
T	Temperature	295 K
P	Hydrostatic Pressure Head	490 Pa

Table S3. Physical parameters employed in finite element simulations.

1b. Finite element procedure

We conduct simulations using the commercial finite element solver COMSOL 5.3a, with the electrostatics, transport of diluted species, and laminar flow physics packages. **Equations S1-S3** are simultaneously evaluated with 2nd (concentration, voltage, velocity) and 1st (pressure) order discretization across mesh elements. The final system contains ~21k rectangular mesh elements resolving the pipette and ~6.5k triangular mesh elements resolving the external solution, with coarse (middle) and high-resolution (right) depictions of pipette meshing shown in **Figure S1**. The ensuing system of linear equations yields ~800k degrees of freedom. Further implementation details are provided in **Supporting Information Part 2**, in the form of a COMSOL model report.

Meshing and geometry at the pipette tip prove crucial to simulation accuracy. Sub-1 nm element lengths are employed at the tip, with meshing of the diffuse part of the double layer chosen such that a minimum of twenty rectangular elements span the region and accurately capture the large gradients. Numerical investigation of various approaches for evaluating nonlinear EOF has shown that meshing of the double layer yields the most accurate solutions.[3] To prevent numerical singularities, the pipette tip is rounded off with a 1 nm radius of curvature. To avoid further assumptions, particularly regarding the effects of the charged glass tangent to the tip and along the outside of the pipette,[4] the outer pipette wall is explicitly included in the simulation, through immersion in a spherical external solution. All components of the mesh are refined such that further increases in mesh density did not alter the ensuing solutions.

To impose large V, a continuation solver is employed. The solver initially evaluates a small voltage ($V = \pm 10$ mV), then uses the smaller-V result as the initial condition for subsequent evaluation at larger V, with the process iteratively continued until the final V is evaluated. Convergence criteria are satisfied when the global sum of the residual errors (relative tolerance) is less than 10^{-6}, with a typical sweep to 1 V taking ~25 minutes when implementing the MUMPS solver through a RHEL 6 server environment with 128GB of RAM. The Codina stabilization method, using the full equation residual, is required to eliminate numerical instability due to convection-driven transport.

1c. Verifying simulated resistances against analytical solutions

Initial verification of the finite element simulation checks simulated resistances against analytical resistances for a purely conical pipette with uniform electrolyte, given in the long cone limit ($H * \tan(\theta) >> a$) as[5]

$$R_{\text{cone}} = \frac{\rho}{\pi a \tan(\theta)} \quad \text{(S4)}$$

where R_{cone} is resistance, ρ is electrolyte resistivity, a is tip radius, θ is cone angle, and H is pipette height. For this verification, we do not consider surface charge ($\sigma = 0$), ignore Navier-Stokes physics, and apply no concentration gradient ($c_{in} = c_{ex}$), consistent with the analytical derivation.

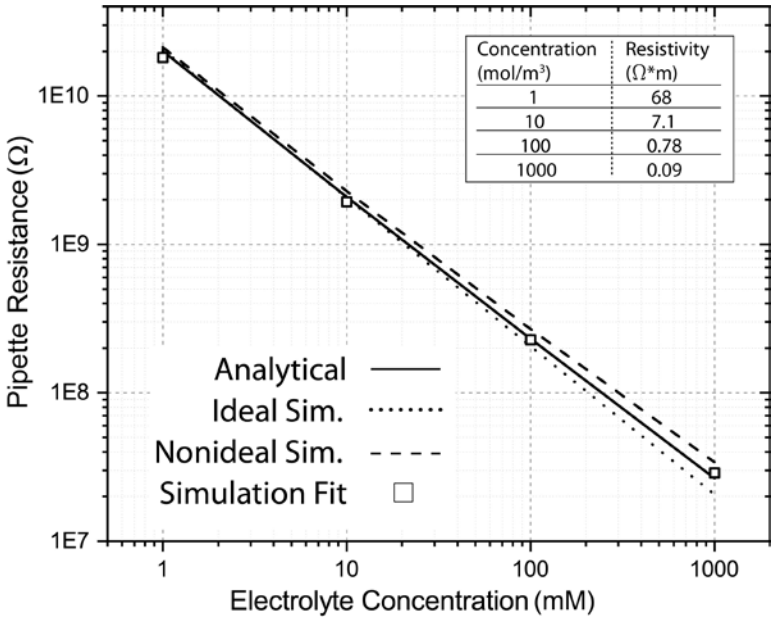

Figure S2. Analytical prediction of concentration-dependent pipette resistance (solid line, **Equation S4**),[5] compared to a thermodynamically ideal simulation (dotted line, using diffusion coefficients in **Table S2**), a nonideal simulation (dashed line, using activity coefficient-corrected diffusion coefficients in **Equation S5**), and a nonideal simulation fit to the analytical results by shortening the simulation geometry (symbols).

Figure S2 depicts the concentration-dependent pipette resistances predicted analytically (solid line, **Equation S4**) and in simulation (dashed, dotted lines). For the analytical evaluation, we use the tabulated resistivity values (inset), where resistivities below 1 M are taken from conductivity-standard KCl solutions (HACH, part numbers: LZW9701.99, LZW9711.99, LZW9721.99), and 1 M resistivity is calculated from the logarithmic scaling of the referenced values. In simulations, we use a cone with a = 12 nm, θ = 5°, and H = 100 μm. Further increases of H negligibly alter solutions, and discrepancies between the dashed and dotted lines are explained below.

For dilute concentrations (< 10 mM), analytical and simulated resistances agree. At higher concentrations, analytical resistances (solid line) are larger than "ideal" simulated resistances (dotted line), due to thermodynamic nonideality of ions in concentrated solutions. To account for this, the diffusion coefficients in **Table S3** are reduced through multiplication by the activity coefficient (γ), based on an empirical modified Debye-Huckel relationship for KCl, given by

$$\log(\gamma) = \frac{-A\sqrt{c}}{1+BS\sqrt{c}} + \beta c + Cc^2 + Dc^3 \qquad \text{(S5)}$$

where γ is activity coefficient, c is concentration, and A, BS, β, C, and D are empirical fitting parameters respectively equal to 0.5108, 1.295, 7 x 10^{-5}, 3.6 x 10^{-3}, and -1.954 x 10^{-4}.[1]

Upon incorporating thermodynamic nonidealities, analytical resistances become smaller than simulated resistances (**Figure S2**, solid versus dashed lines), indicating that this procedure causes the simulation to overcorrect. We attribute this to concentration-dependent resistivity (inset) not exactly scaling as would be predicted using activity coefficient-scaled concentration increases.

We therefore choose to incorporate activity coefficients and fit the simulation geometry to quantitatively agree with the high-concentration analytical values, through reducing H. The square symbols show this fitting based on nice overlap with the solid line (**Figure S2**), where symbols represent simulated resistances from a model incorporating a shortened pipette cone (H = 0.75 μm) and thermodynamic nonidealities. We note that so long as $H >> a$, reducing H does not affect global physics, such that when comparing solutions with H = 100 μm and H = 0.75 μm, resistance reduces by < 20% and results are qualitatively consistent.

1d. Fitting simulation geometry to experimental data in Figure 1b

We implement a similar fitting procedure to determine the geometry of a pipette including a short cylindrical region at the tip and an external solution, which is more representative of experimental conditions. Considering new contributions to resistance, we modify **Equation S4** to respectively add the cylindrical resistor and external access resistance terms in series with the conical resistor,

$$R_{\text{pip}} = \frac{\rho}{\pi a \tan(\theta)} + \frac{\rho}{\pi h a^2} + \frac{\rho}{4a} \qquad \text{(S6)}$$

where R_{pip} is pipette resistance and h is the height of the cylindrical region at the pipette tip.

When c_{in} = c_{ex} = 3 M, R_{pip} = 14 MΩ is experimentally recorded (**Figure 1b**, dashed line). This experimental R_{pip} is analytically fit to a pipette with a = 12 nm, θ = 5°, h = 50 nm, and ρ = .033 Ω*m (where ρ is determined based on the scaling of the values in the **Figure S2** inset). The analytical and simulated resistances, using the four approaches of **Figure S2**, are listed in **Table S4**, where R_{an} solves **Equation S6** as described, R_{sim} corresponds to a thermodynamically ideal simulation, R_{sim}' adds activity coefficient-scaling of diffusion coefficients, and R_{sim}***** shortens the

pipette cone. For a pipette measured in c_{in} = c_{ex} = 3 M KCl (γ = .565), a short cone with H = 0.5 μm closely matches the experimental result of **Figure 1b** (R_{sim}***** = 14.1 MΩ).

[KCl] (M)	R_{an}	R_{sim}	R_{sim}'	R_{sim}*
3	14 MΩ	9.5 MΩ	16.8 MΩ	14.1 MΩ

Table S4: Fitting analytical and simulated pipette resistances to experimental data of **Figure 1b,** when c_{in} = c_{ex} = 3 M. With a = 12 nm, θ = 5°, h = 50 nm, and ρ = .033 Ω*m, analytical resistance matches the experimental value (R_{pip} **=** R_{an} = 14 MΩ). A thermodynamically ideal simulation (R_{sim}) underestimates resistance, while correcting diffusion coefficients through activity coefficient-scaling (R_{sim}') overestimates resistance. Upon shortening pipette height (H = 0.5 μm), a simulation including activity coefficients quantitatively matches experimental data (R_{sim}***** ≈ R_{pip}).

1e. Incorporating activity coefficients with concentration gradients

When c_{in} = c_{ex}, a single global activity coefficient could be applied as a correcting factor to the ideal diffusion coefficient. When c_{in} ≠ c_{ex}, the activity coefficient varies spatially. We thus introduce a spatially dependent diffusion coefficient function, $D'(z) = \gamma(z)*D$, where D' is the concentration-dependent diffusion coefficient, γ is the local activity coefficient, and D is the ideal diffusion coefficient (**Table S3**). To implement this, we measure the centerline concentration during solver operation and adjust the diffusion coefficient in a radially-independent manner according to **Equation S5**. Locally varying the diffusion coefficients did not qualitatively change simulation results, only the magnitudes of simulated currents.

1f. Verifying evaluation of double layer physics

Based on the agreement between analytical and simulated resistances in **Figure S2**, we confirm accurate simulation of P-NP physics. Upon adding surface charge, we verify accurate simulation of double layer physics through analysis of the simulated EOF velocity. When EOF is linear, electrostatic shearing forces in the double layer induce bulk fluid flow according to the Smoluchowski relation, $u_{eo} = \sigma E/\eta\kappa$,[6] where E is voltage gradient and the substitution $\zeta = \sigma/\varepsilon\kappa$[7] has been employed (where ζ is zeta potential). To verify accurate EOF, we consider the simulation of **Figure 1b** (squares), noting that when c_{in} = c_{ex} = 3 M and V = 0.5 V, EOF is linear (**Figure 3c**). In **Figure S3**, we show quantitative agreement between the Smoluchowski velocity calculation (symbols) and the simulated velocity (curve), where simulated velocity is measured along the

centerline of the finite element model and the Smoluchowski calculation uses the simulated local voltage gradient, the applied surface charge (σ = -8 mC/m^2), and the Debye length for a 3 M solution (κ^{-1} = 0.18 nm).

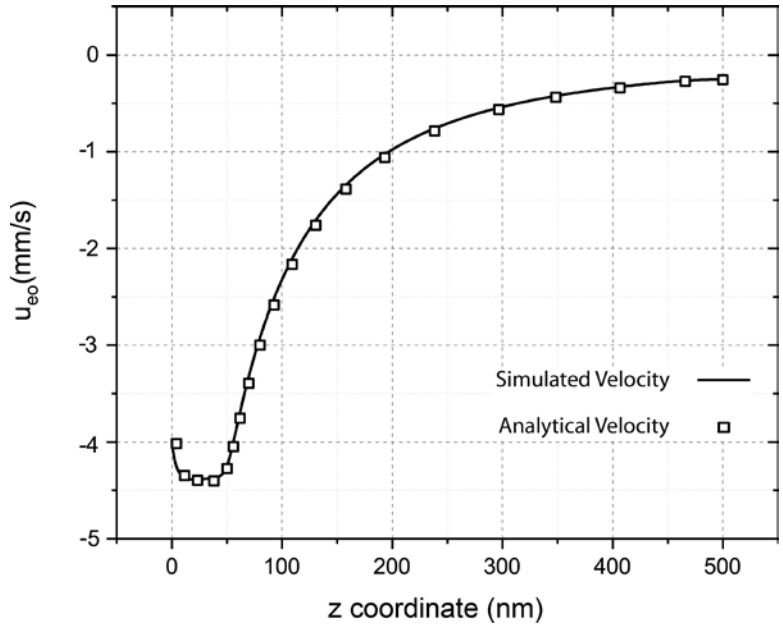

Figure S3. Simulated EOF velocity (curve) versus analytical EOF velocity (symbols, $u_{eo} = \sigma E/\eta\kappa$[6,7]) under linear EOF conditions ($c_{in} = c_{ex}$ = 3 M, V = 0.5 V). Agreement indicates that double layer physics are accurately simulated.

1g. Verifying fluid and mass continuity

The final step in simulation verification is ensuring continuity in volumetric fluid flow and ion flux across the top of the pipette, the tip of the pipette, and the edge of the external solution. Though global continuity is not explicitly constrained in the governing equations, it must be an outcome of an accurate steady state simulation. Initially, we observe moderate discrepancies (~10%) in continuity that could not be overcome through finer meshing or higher order equation discretization. The inaccuracy is caused by inconsistency in the boundary conditions at the top corner of the pipette, where the nonzero surface charge on the glass results in double-layer voltage and concentration distributions, but constant-valued boundary conditions are imposed. We therefore explicitly include Gouy-Chapman distributions within the boundary conditions atop the pipette, according to the expressions

$$V_{\mathrm{DL}}(x) = V + 2V_{\mathrm{T}} \ln\left[\frac{1+\alpha e^{-\kappa x}}{1-\alpha e^{-\kappa x}}\right] \qquad \text{(S7)}$$

$$c_{\mathrm{DL}}(x, z_i) = c_{\mathrm{in}} \exp\left[\frac{-z_i V_{\mathrm{DL}}(x)}{V_{\mathrm{T}}}\right] \quad \text{(S8)}$$

$$\alpha = \frac{\exp\left[a\, sinh\left(\frac{\sigma}{\sqrt{8N_A \varepsilon k_B T c_{\mathrm{in}}}}\right)\right] - 1}{\exp\left[a\, sinh\left(\frac{\sigma}{\sqrt{8N_A \varepsilon k_B T c_{\mathrm{in}}}}\right)\right] + 1} \quad \text{(S9)}$$

where V_{DL} is the double layer voltage, x is radial distance from the charged glass wall, V_{T} is thermal voltage, and c_{DL} is the double layer concentration. Upon imposing the Gouy-Chapman boundary conditions as given in **Equations S7-S9**, continuity is maintained for fluid flow and ion fluxes, with < 1% discrepancy in fluid flow and mass flux across the aforementioned boundaries.

1h. External pressure from fluid-filled capillary does not influence simulation results

Experimentally, a hydrostatic pressure (**Figure S1**, $P \approx 0.5$ kPa) exists above pipette tips due to the ~5 cm long solution column filling the vertically-oriented pipette. Prior work has demonstrated the influence of pressure-driven flow on ICR[8] and NDR,[9] so we apply a pressure (P) in our simulations for completeness. We simulate whether this small pressure contributes to the experimental results by sweeping it from 0 to 100 kPa. The corresponding current-voltage measurements are provided in **Figure S4**. Below 10 kPa, we observe no change in the behavior of the system. Linearization of ICR occurs at 100 kPa. Thus, the effects we observe are insensitive to the hydrostatic pressure or the precise level of the solution filling the pipette.

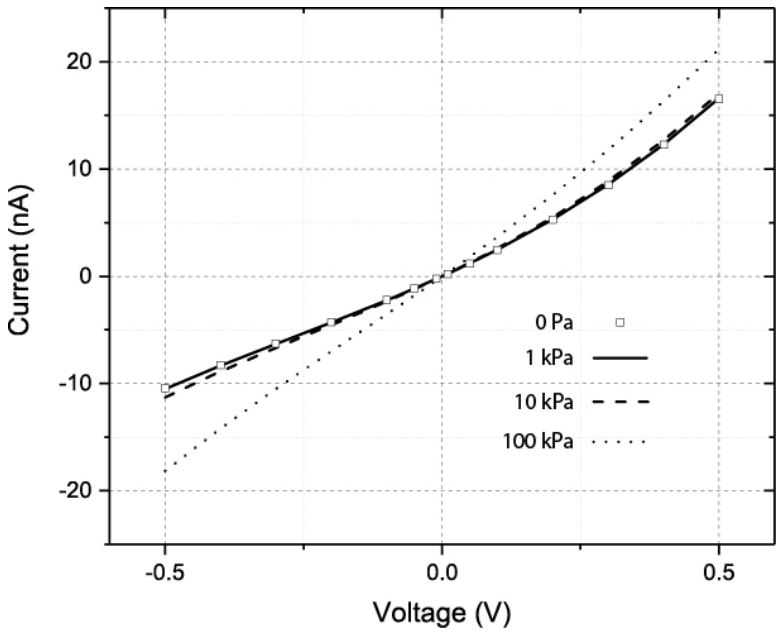

Figure S4. Simulated current-voltage relations when varying external pressure. Hydrostatic pressure during experimentation (~0.5 kPa) does not influence physics.

2. Experimental pipette characterization

2a. Outward ICR when $c_{in} > c_{ex}$

In **Figure 1b**, we show a nanopipette to exhibit a linear current-voltage relation when $c_{in} = c_{ex} = 3$ M and outward ICR when $c_{in} = 3$ M and $c_{ex} = 140$ mM. **Figure S5** shows the reproducibility of this behavior across five additional pipettes. **Figure S5a** depicts recordings when $c_{in} = c_{ex} = 3$ M (compare to **Figure 1b**, dashed line), with color-coded pipette resistances (R_{pip}) listed and independent of voltage. High-κa conditions are satisfied because no ICR is recorded. Surface charge and EOF contribute negligibly to conductivity (**Figure S18**) such that variability in R_{pip} is attributed to geometric variations during pipette fabrication.

Figure S5b depicts recordings when $c_{in} = 3$ M and $c_{ex} = 140$ mM (compare to **Figure 1b**, solid curve), where R_{pip} varies with voltage and is calculated from linearization of current recordings around $V = \pm 0.5$ V. The current rectification ratio (RR) quantifies ICR based on the ratio of the larger current over the smaller current at $V = \pm 0.5$ V. RR generally increases with R_{pip} (**Figure S5b**, table), though variability arises from the different influences of pipette parameters (**Figure S1**) on conductivity

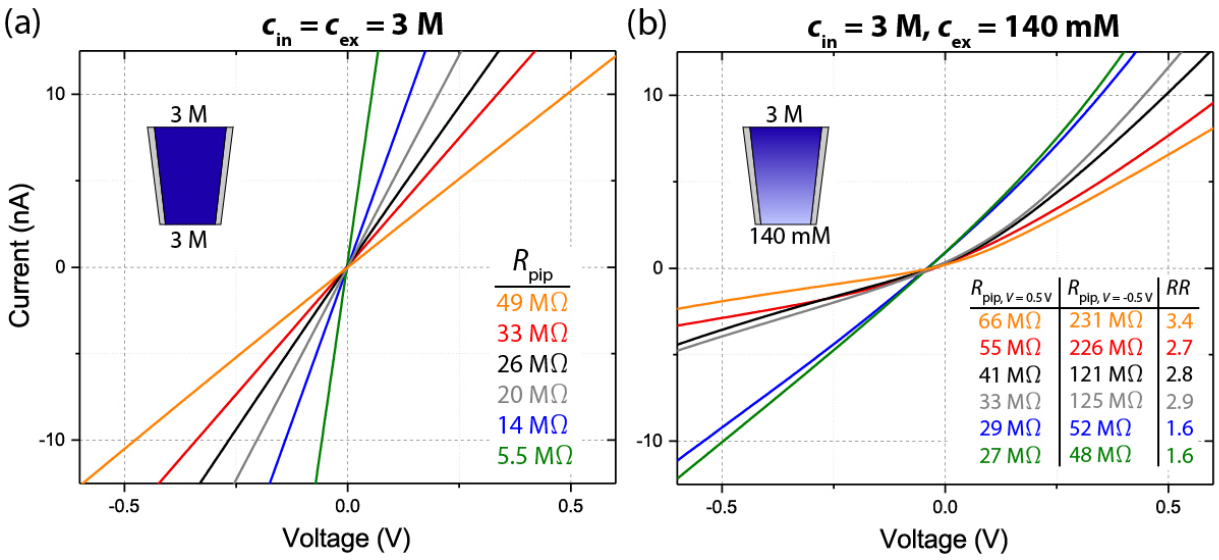

Figure S5. Current-voltage recordings from six pipettes when (a) $c_{in} = c_{ex} = 3$ M and (b) $c_{in} = 3$ M and $c_{ex} = 140$ mM. Color-coded resistance values are calculated around $V = \pm 0.5$ V and correspond to curves and voltages as indicated. Blue (**Figure 1b**) and orange (**TOC graphic**) curves redisplay data. (b) Pipettes consistently show outward ICR when $c_{in} > c_{ex}$.

2b. Inward ICR under low-κa conditions when $c_{in} = c_{ex}$

We confirm that our glass pipettes have negatively charged surfaces based on experimental recordings under low concentration and $c_{in} = c_{ex}$ conditions. Shown in **Figure S6** are current-voltage recordings for three separate pipettes, measured when $c_{in} = c_{ex}$ = 3 mM (red), 30 mM (blue), and 300 mM (black). Color-coded *RR* values are listed at each concentration. Inward Debye-overlap ICR is observed, consistent with prior reports.[4,10]

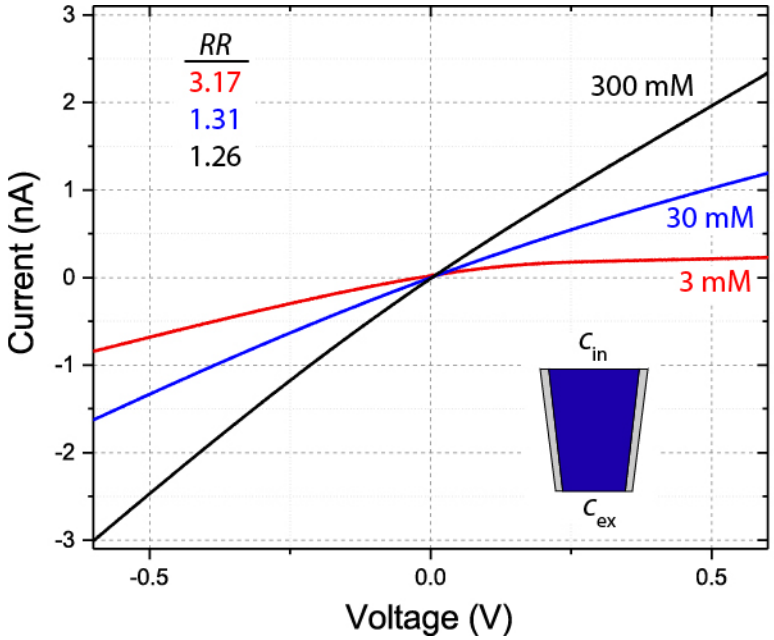

Figure S6. Current-voltage recordings from three separate pipettes, measured when $c_{in} = c_{ex}$ = 3 mM (red), 30 mM (blue), and 300 mM (black). Inward ICR under low-*κa* and $c_{in} = c_{ex}$ conditions confirms glass pipettes to have negatively charged surfaces.

2c. Determining concentration ranges for high-κa and low-κa conditions

To rule out Debye-overlap ICR as governing our experimental results, we examine how R_{pip} and *RR* scale with concentration. From these results, we determine the concentration range where our experimental system transitions from high-*κa* to low-*κa* conditions. We determine a transitional concentration range through two indications: (1) *RR* converges to 1 under $c_{in} = c_{ex}$ and high-*κa* conditions, and (2) R_{pip} is governed by electroneutral solution conductivity under high-*κa* conditions and by double layer space charge conductivity under low-*κa* conditions.[11,12]

In **Figure S7**, we show average *RR* (gray bars, left axis) and R_{pip} (red symbols, right axis) versus concentration for pipettes measured under $c_{in} = c_{ex}$ conditions. We calculate R_{pip} at V = -0.5 V. Reported values are averages across N pipettes, with $N = \{3, 3, 5, 6\}$ for 3 mM, 30 mM, 300 mM, and 3 M, respectively; error bars depict standard deviations. Pipettes exhibit *RR* = 3.1 in 3 mM solutions, with *RR* decreasing upon increasing concentration and converging to *RR* = 1 (no ICR) in 3 M solutions. The slight ICR at 300 mM and loss of ICR at 3 M suggest a transition to high-κa conditions between 300 mM and 3 M. Similarly, we measure a 10-fold increase in R_{pip} when reducing concentration from 3 M (R_{pip} = 25 MΩ) to 300 mM (R_{pip} = 260 MΩ), consistent with high-κa conditions, where bulk solution conductivity governs R_{pip}. Below 300 mM, equal reductions in concentration yield smaller increases in R_{pip}, consistent with low-κa conditions, where double layer space charge conductivity governs R_{pip}.[11,12]

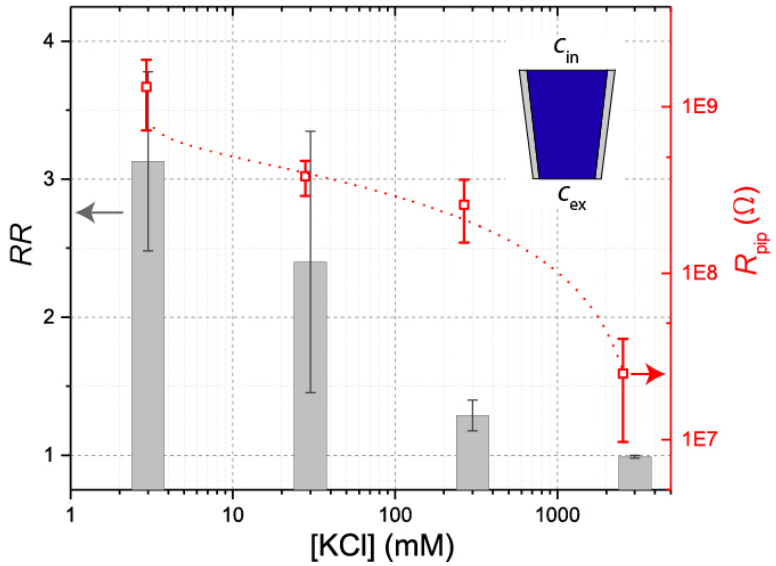

Figure S7. Concentration-dependent scaling of *RR* (gray bars) and R_{pip} (red symbols), when $c_{in} = c_{ex}$. Red line is a fit of R_{pip} vs concentration data. Because *RR* = 1 at 3 M and *RR* > 1 at 300 mM, the average pipette transitions from high-κa to low-κa conditions between 3 M and 300 mM.

2d. Tunable ICR when varying concentration gradient direction

Prior reports of EOF-governed ICR demonstrate tunability in ICR direction and magnitude through modification of the concentration or viscosity gradient.[13–15] In **Figure S8**, we observe this effect across three current-voltage recordings from a single pipette filled with c_{in} = 1 M solution and measured in c_{ex} = 1 M (black), 3 M (red), and 1/3 M (blue) solutions. We observe weak inward ICR when $c_{in} = c_{ex}$ (black curve, *RR* = 1.2), stronger inward ICR when $c_{in} < c_{ex}$ (red curve, *RR* = 1.6), and outward ICR when $c_{in} > c_{ex}$ (blue curve, *RR* = 1.3).

We note that inward ICR could not be induced for a pipette when c_{in} = 3 M, as the limit of KCl solubility in water precludes a $c_{in} < c_{ex}$ condition when c_{in} = 3 M.

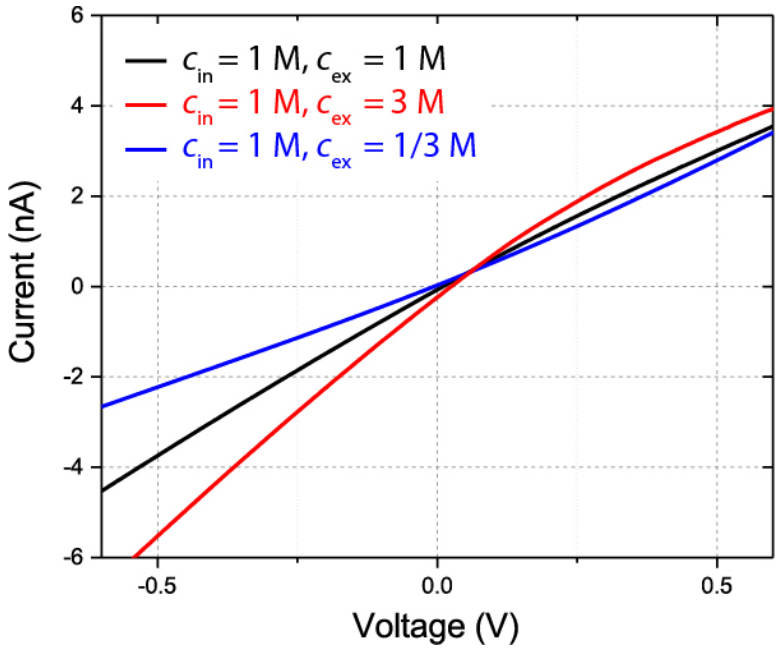

Figure S8. Current-voltage recordings from a single pipette filled with c_{in} = 1 M solution and measured in c_{ex} = 1 M (black), 3 M (red), and 1/3 M (blue) solutions. Inversion from inward ICR ($c_{in} = c_{ex}$, black; $c_{in} < c_{ex}$, red) to outward ICR ($c_{in} > c_{ex}$, blue) demonstrates tunability of flow ICR.

3. Nonlinear EOF and fluid continuity cause vortex flow patterns

3a. Concentration gradient induces nonlinear EOF near pipette walls

We attribute the centerline flow reversals of **Figures 2a,b** to fast EOF along the pipette sidewalls and fluid continuity constraints. We quantify these effects in **Figure S9**, which depicts simulated velocity profiles along the pipette centerline (solid curves, r = 0) and along an axis parallel to and 1 nm away from the sidewalls (**Figure S9b,** dotted curves, $r = a(z) - 1$ nm) for the pipette in **Figure 1b** when c_{in} = 3 M, c_{ex} = 140 mM, and V = ± 0.5 V.

Centerline and sidewall EOF velocities in **Figure S9** indicate linear EOF far from the tip and nonlinear EOF near the tip. Progressing from the simulation boundary (z = 500) nm to the pipette tip (z = 0 nm), centerline velocities increase due to a reducing pipette cross-section and fluid continuity constraints. In the distal region, linear EOF prevails, based on flow being fastest at the

centerline and slower near the sidewalls (**Figure S9b**) due to the no-slip boundary condition. Towards the tip, nonlinear EOF manifests in rapidly increasing sidewall velocities, and centerline velocities correspondingly reduce to preserve fluid continuity. When the nonlinear EOF becomes sufficiently fast, fluid continuity induces centerline flow reversals, as indicated by the curves crossing the dashed blue line (**Figure S9a**).

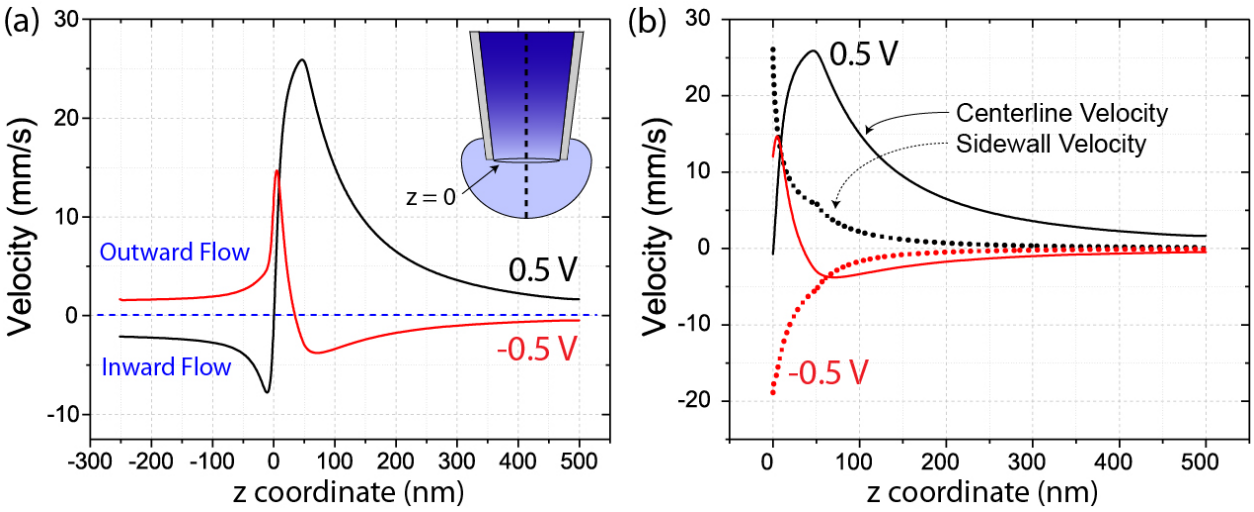

Figure S9. Simulated (a,b) centerline (r = 0, solid curves) and (b) sidewall ($r = a(z) - 1$ nm, dotted curves) velocity distributions for the pipette of **Figure 1b**, when c_{in} = 3 M, c_{ex} = 140 mM, and V = ± 0.5 V. (a) Centerline flows reverse directions where curves cross dashed blue lines. (b) Reversed flows develop to maintain continuity in volumetric fluid flow amidst faster EOF along sidewalls.

When the concentration gradient is removed, the double layer becomes uniform across the pipette and nonlinear EOF becomes negligible. As a result, the discrepancy between centerline and sidewall velocities depicted in **Figure S9b** does not develop. Shown in **Figure S10** are simulated velocity profiles for $c_{in} = c_{ex}$ = 3 M (left) and $c_{in} = c_{ex}$ = 140 mM (right) conditions. In the absence of a concentration gradient, sidewall velocities do not exceed centerline velocities (ignoring a negligible "corner effect" at the tip, when $c_{in} = c_{ex}$ = 3 M), nonlinear EOF is insignificant, and neither vortex flow patterns nor centerline flow reversals develop.

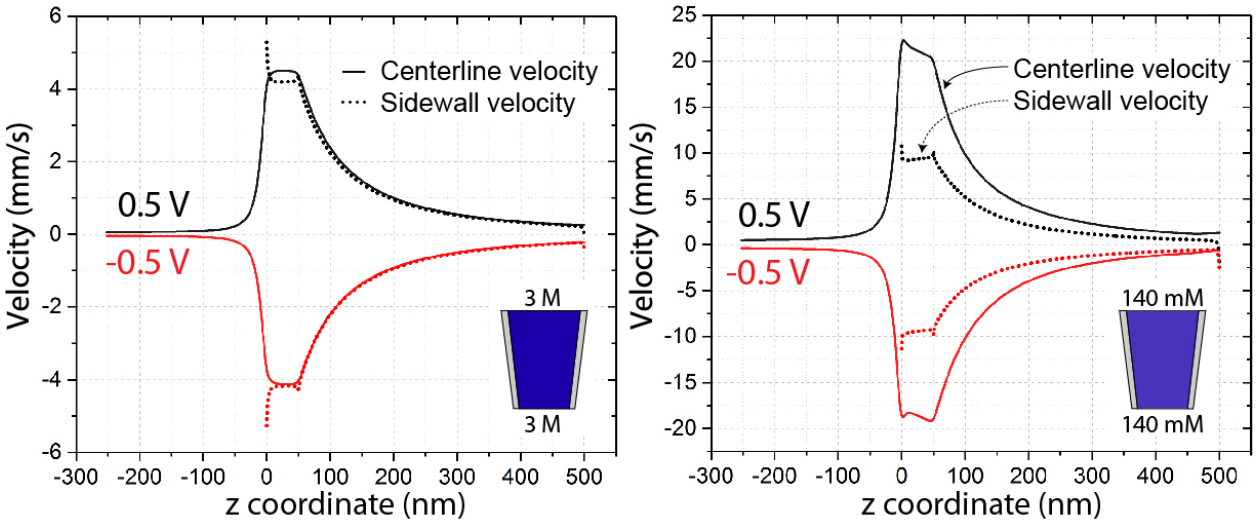

Figure S10. Simulated centerline (r = 0, solid curves) and sidewall ($r = a(z) - 1$ nm, dotted curves) velocity profiles, for $c_{in} = c_{ex}$ = 3 M (left) and $c_{in} = c_{ex}$ = 140 mM (right) conditions, at $V = \pm$ 0.5 V. Without a concentration gradient, centerline velocities exceed sidewall velocities throughout the pipette (ignoring negligible tip effect when $c_{in} = c_{ex}$ = 3 M). Under high-κa conditions (left), radial velocity profiles settle across a distance < 1 nm; under low-κa conditions (right), radial velocity profiles settle across a distance > 1 nm, explaining discrepancy in curve spacing.

3b. Concentration gradient increases EOF velocity

Due to nonlinear EOF, the concentration gradient increases the maximum simulated EOF velocity inside the pipette. Shown in **Figure S11** are the maximum simulated velocities for the pipette of **Figure 1b**, with (c_{in} = 3 M, c_{ex} = 140 mM) and without ($c_{in} = c_{ex}$ = 140 mM and $c_{in} = c_{ex}$ = 3 M) a concentration gradient. Nonlinear EOF increases velocity in the presence of a concentration gradient, as compared to both uniform concentration conditions. Slight EOF rectification occurs in uniform concentration conditions, consistent with prior works.[16]

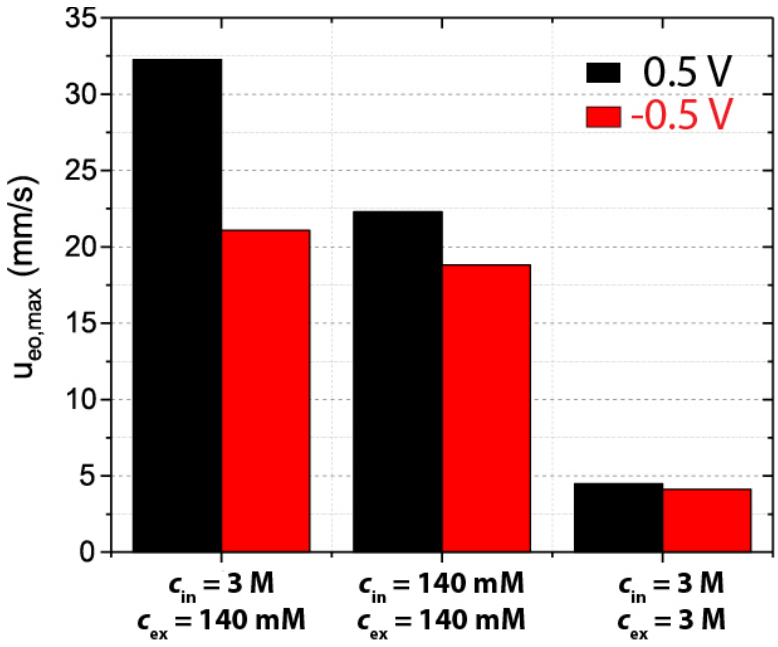

Figure S11. Maximum simulated EOF velocity ($u_{eo,max}$) for the pipette of **Figure 1b** under various concentration conditions, when V = ±0.5 V. The concentration gradient induces nonlinear EOF, increasing the maximum velocity as compared to uniform concentration conditions.

3c. Internal hydrostatic pressures drive reversed fluid flows

We observe that large internal hydrostatic pressures develop to support the centerline flow reversals in **Figures 2a,b** and **S9a**. Shown in **Figure S12** are centerline pressure profiles for the pipette of **Figure 1b**, when c_{in} = 3 M, c_{ex} = 140 mM, and V = ± 0.5 V. The combination of fast EOF at the tip and fluid continuity constraints induces internal hydrostatic pressures that far exceed the gravity-induced pressure head (~ 0.5 kPa). As a result, the external pressures in **Figure S4** do not influence pipette transport until they are comparable to the internal pressures quantified in **Figure S12**. The faster EOF for V = 0.5 V than for V = -0.5 V (**Figures S9a** and **S11**) requires larger pressures to induce flow reversal.

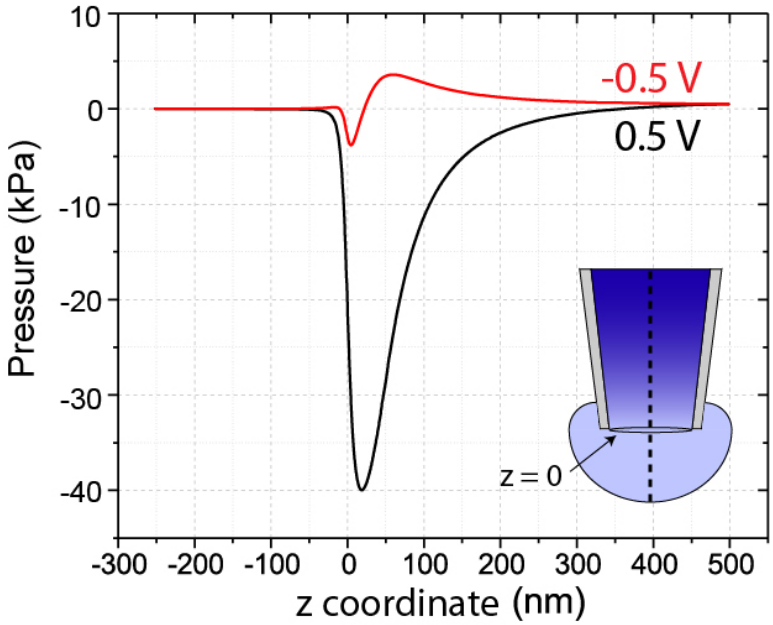

Figure S12. Simulated centerline pressure profiles for the pipette of **Figure 1b**, when c_{in} = 3 M, c_{ex} = 140 mM, and V = ± 0.5 V. Large hydrostatic pressures develop to drive reversed centerline flows, which we correspondingly refer to as hydrostatic back flows.

3d. Charge polarization at pipette tip confirms ICEO mechanism for nonlinear EOF

To verify ICEO as the nonlinear EOF mechanism, we quantify sidewall charge polarization at the tip of the pipette in **Figure 1b**, when c_{in} = 3 M, c_{ex} = 140 mM, and V = ± 0.5 V. Charge polarization is approximated in terms of an effective surface charge, $\sigma_{effective} = \varepsilon\zeta(z)/\kappa^{-1}(z)$[7], where we determine the local zeta potential (**Figure 3a**, inset) and Debye length from the simulation. We thus approximate the effective surface charge and compare it to the nominal value imposed as a boundary condition ($\sigma_{nominal}$ = -8 mC/m^2).

We depict sidewall charge polarization in **Figure S13**, where effective surface charge scales in a manner consistent with the zeta potential profiles in **Figure 3a**. Charge polarization occurs at any geometric "corner," explaining the return to the nominal value in the cylindrical region of the tip ($z \approx 30$ nm) and the zeta potential hitches observed at this interface in **Figure 3a** (z = 50 nm). The magnitude of charge polarization is mostly independent of voltage polarity and increases with voltage magnitude. The concentration gradient serves to amplify the induced zeta potential nonuniformity and resulting ICEO flow, as similar effective surface charge profiles develop when $c_{in} = c_{ex}$ = 3 M and $c_{in} = c_{ex}$ = 140 mM, yet the influence of EOF on transport in these cases is minimal (**Figure S18**).

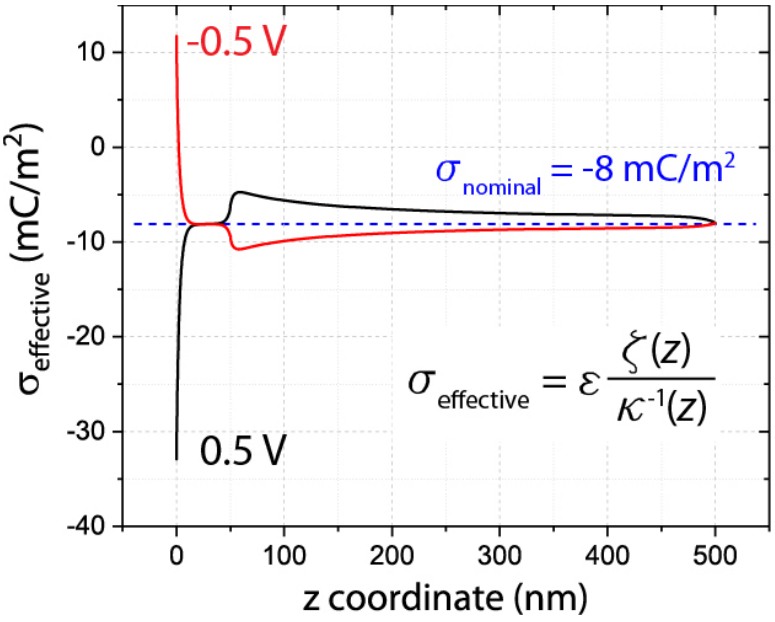

Figure S13. Simulated effective surface charge [$\sigma_{effective} = \varepsilon\zeta(z)/\kappa^{-1}(z)$[7]] for the pipette of **Figure 1b**, when c_{in} = 3 M, c_{ex} = 140 mM, and V = ± 0.5 V. Effective surface charge differs from nominal surface charge imposed as a boundary condition ($\sigma_{nominal}$ = -8 mC/m^2, dashed blue line), due to charge polarization of the glass pipette sidewalls, consistent with the ICEO mechanism for nonlinear EOF.

Radial concentration profiles at the pipette tip support the induced charge polarization shown in **Figure S13**. In **Figure S14**, K^+ (green curves) and Cl^- (blue curves) concentrations are plotted across the radius at the pipette tip (z = 0 nm) for V = 0.5 V (solid curves) and V = -0.5 V (dashed curves). Coinciding with the polarity inversions in zeta potential and surface charge (**Figures 3a** and **S13**, red curves), the electrolyte at the pipette tip becomes slightly anion-rich when V = -0.5 V. Upon integrating the dashed curves in **Figure S14**, we find 0.7% more Cl^- than K^+ along the radial axis at the pipette tip.

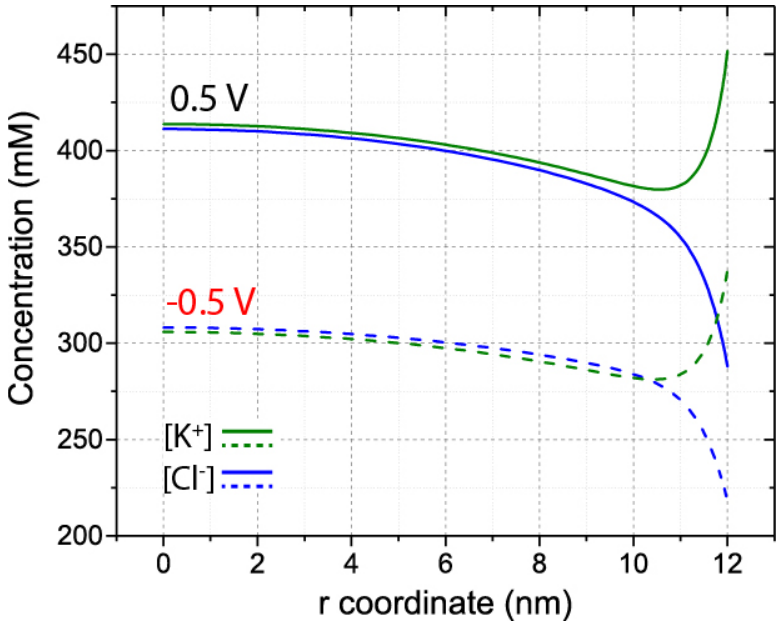

Figure S14. Simulated radial concentration profiles for the pipette of **Figure 1b**, when c_{in} = 3 M, c_{ex} = 140 mM. At V = 0.5 V (solid curves), cation concentration (green curves) exceeds anion concentration (blue curves). At V = -0.5 V (dashed curves), induced charge polarization inverts the ionic charge distribution such that anions exceed cations.

4. Comparison of flow ICR and Debye-overlap ICR

4a. Ion concentration enrichment and depletion during Debye-overlap ICR

Ion concentration polarization, via enrichment or depletion, is shared between flow ICR (**Figure 4**) and Debye-overlap ICR (**Figure S15a**). In **Figure S15**, we show simulated centerline ion distributions for the Debye-overlap ICR conditions in **Figure S6** (red curve, $c_{in} = c_{ex}$ = 3 mM). We observe voltage-dependent enrichment (V < 0 V, red curve) and depletion (V > 0 V, black curve) of the average concentration, calculated as ($[K^+] + [Cl^-]$) / 2. At higher concentrations, Debye-overlap ICR can occur while centerline electroneutrality is maintained, provided that a significant space charge exists between the centerline and the channel wall.

Figure S15b redisplays the gray curve of **Figure S15a** alongside the K^+ (black curve) and Cl^- (red curve) concentrations composing the average (gray). The presence of a space charge electrolyte ($[K^+] \neq [Cl^-]$) contrasts high-κa flow ICR, where a bulk electroneutral solution persists (**Figure 4**). At higher concentrations, the curves of **Figure S15b** would collapse into a flat line, reducing space charge to zero and eliminating ICR. The analog to flow ICR would be elimination of the solution asymmetry.

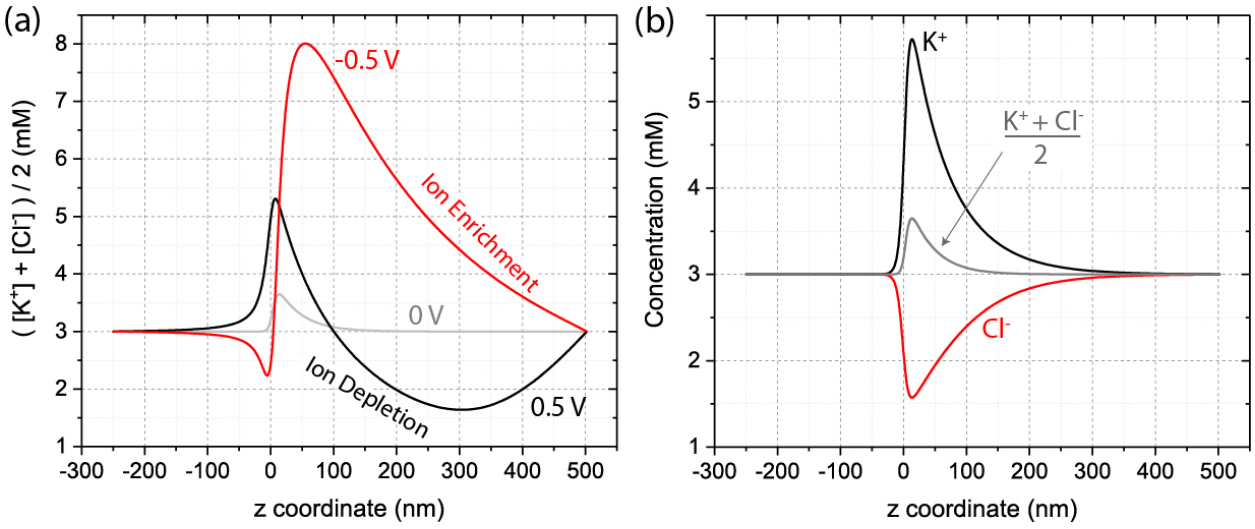

Figure S15. Simulated centerline ion distributions for the Debye-overlap ICR conditions of **Figure S6** (red curve, $c_{in} = c_{ex} = 3$ mM). (a) Average centerline concentration, showing voltage-dependent enrichment (V = -0.5 V, red curve) and depletion (V = 0.5 V, black curve), compared to V = 0 V (gray curve). (b) Ion composition when V = 0 V. K^+ (black curve) and Cl^- (red curve) concentrations show space charge electrolyte underlying Debye-overlap ICR.

4b. Ion transport selectivity is tunable during flow ICR and fixed during Debye-overlap ICR

We simulate voltage-dependent pipette permselectivity with the transference number (t^+), defined as the fraction of the pipette current comprised by cations.[17] **Figure S16** shows simulated t^+ during flow ICR (solid curve) based on the pipette of **Figure 1b**, and simulated t^+ during Debye-overlap ICR (dotted curve), based on the conditions of **Figure S6** (red curve, $c_{in} = c_{ex} = 3$ mM). The flow ICR pipette shows tunable permselectivity (**Figure S16**, solid curve), preferentially transporting cations when $V > 0$ V and anions when $V < 0$ V. In contrast, the Debye-overlap ICR pipette is always permselective for cations (dotted curve), due to space charge electrolyte within the negatively charged tip.

During flow ICR, the concentration gradient enables tunable permselectivity. When $c_{in} > c_{ex}$, ions diffuse from the pipette. When $V \neq 0$ V, one ion species will be drawn into the pipette through voltage-driven transport. If voltage magnitude is chosen such that the voltage-driven influx closely matches the diffusive efflux, net transport of the relevant ion is minimized and the channel selectively transports the other ion, as seen previously.[18]

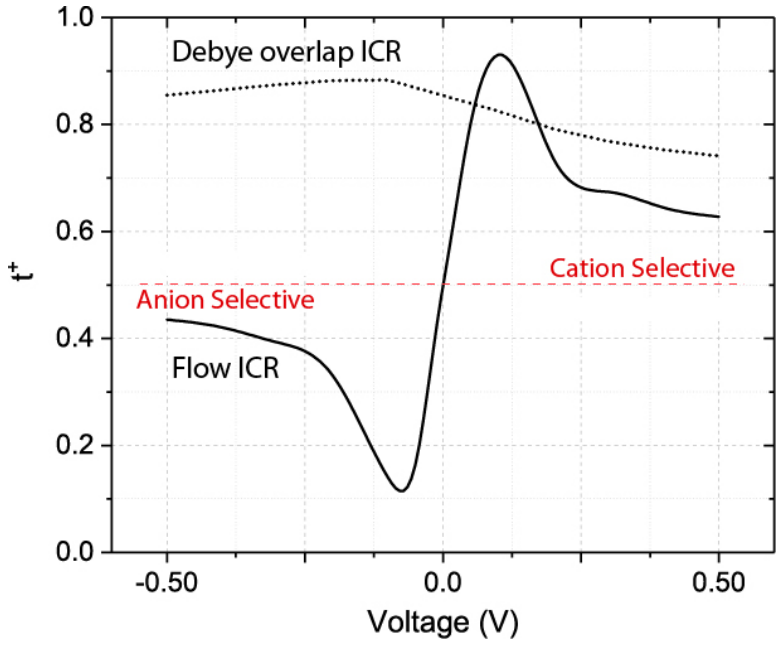

Figure S16. Simulated voltage-dependent ion selectivity (t^+) for the pipette of **Figure 1b**, when c_{in} = 3 M and c_{ex} = 140 mM (solid curve), and the conditions of **Figure S6**, when c_{in} = c_{ex} = 3 mM (dotted curve). Ion selectivity is quantified by the transference number (t^+), calculated as the fraction of the current comprised by cations. Under experimental conditions, the flow ICR pipette shows tunable permselectivity; the Debye-overlap ICR pipette is always permselective for cations.

Experimental evidence further supports anion selectivity at negative voltages during flow ICR. In **Figure S5b**, the average voltage where zero current is recorded is -32.5 mV. From this voltage, we can determine the selectivity of the pipette after correcting for the built-in Nernst potential difference due to the concentration gradient[19,20] (equal to 67.5 mV when considering KCl activity coefficients). The corrected zero-current voltage of 35 mV is used to evaluate selectivity according to the relationship

$$\Delta V = (2t^+ - 1)\frac{RT}{F}\ln\left(\frac{\gamma_{ex}c_{ex}}{\gamma_{in}c_{in}}\right) \qquad \text{(S10)}$$

where ΔV is the corrected zero-current voltage and γ is activity coefficient. Using ΔV = 35 mV, we calculate t^+ = 0.25 for the experimental data in **Figure S5b**, demonstrating that when V = -32.5 mV, the current consists of 75% anions. The experimental result agrees closely with the simulation result in **Figure S16**.

5. EOF influences transport amidst concentration gradients

In **Figure S17,** we extend **Figure 5** across a wider range of concentration gradients by simulating current-voltage relationships with EOF (P-NP-NS, black curves) and without EOF (P-NP, red curves), using the model of **Figure 1b** (with the slight change of σ = -10 mC/m^2). We depict the error introduced by ignoring EOF based on the change in *RR*. Each panel in **Figure S17** corresponds to a single c_{in} condition, while c_{ex} is varied across the 3 mM – 3 M concentration range; *RR* is the ratio of current at V = 0.5 V over current at V = -0.5 V, *RR* > 1 indicates outward ICR, and *RR* < 1 indicates inward ICR. We observe significant quantitative and qualitative disagreement throughout the simulations when ignoring EOF, demonstrating that EOF must be considered in order to properly model transport under concentration gradients.

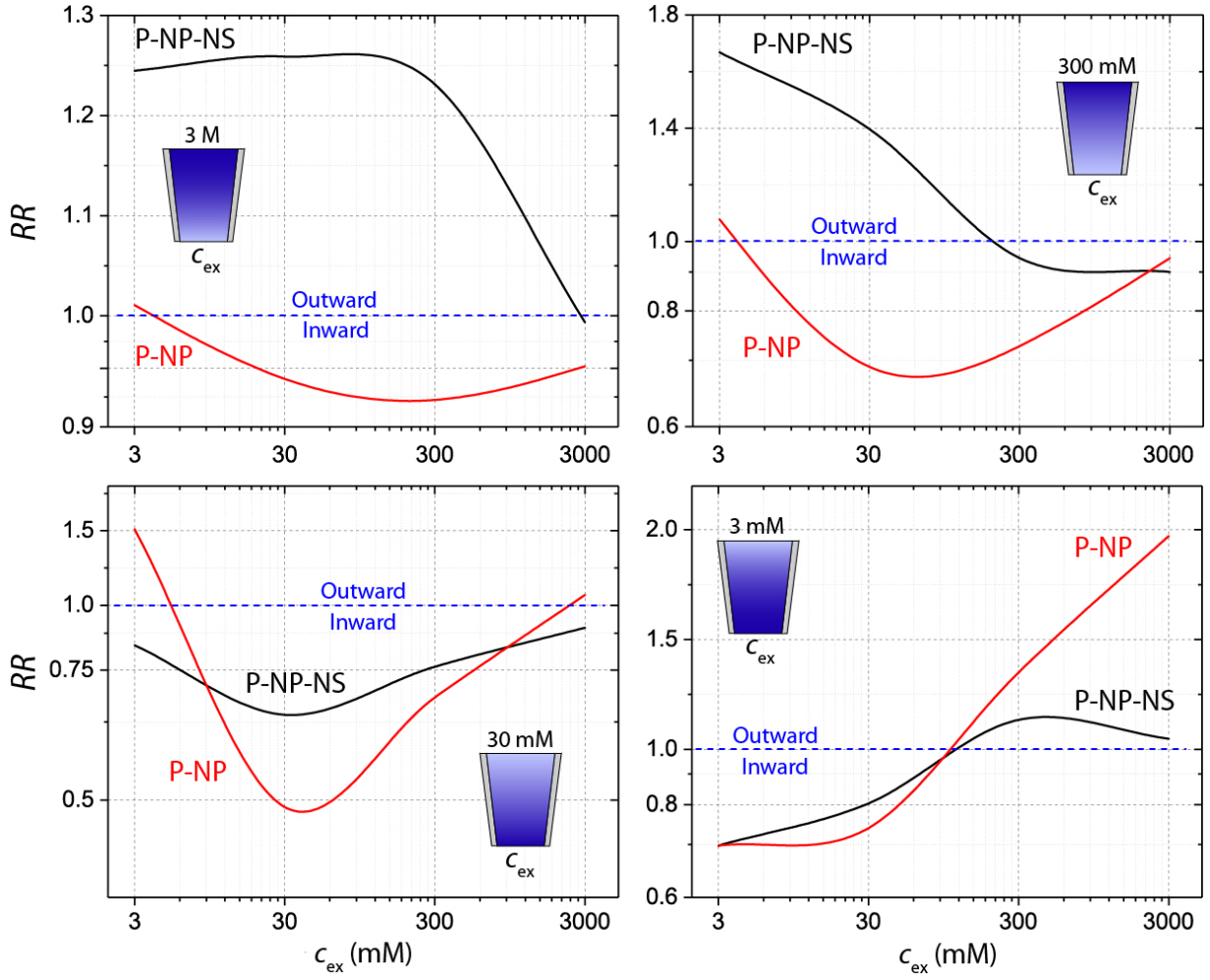

Figure S17. Simulated *RR* under concentration gradients, based on the numerical model of **Figure 1b**, simulated with EOF (P-NP-NS, black curves) and without EOF (P-NP, red curves). Each graph represents a single c_{in} value, evaluated across varying c_{ex}. Quantitative discrepancies between the

P-NP-NS and P-NP curves demonstrate the need to consider EOF when modeling nanochannel transport amidst concentration gradients.

Figure S18 shows the validity of ignoring EOF when $c_{in} = c_{ex}$,[4] based on simulated pipette current-voltage relationships using the numerical model of **Figure 1b**. When $c_{in} = c_{ex} = 3$ M (left) and $c_{in} = c_{ex} = 140$ mM (right), simulations considering EOF (symbols) and ignoring EOF (curves) qualitatively agree, with small quantitative errors only at the limits of large voltage and surface charge, when $c_{in} = c_{ex} = 140$ mM.

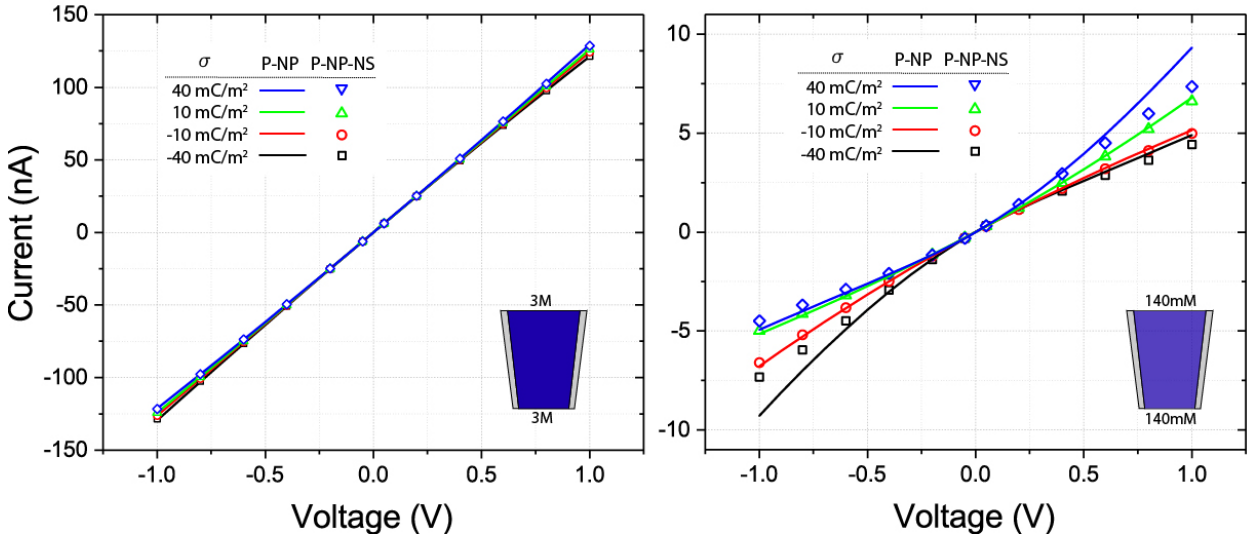

Figure S18. Simulated pipette current-voltage relationships in the absence of concentration gradients, based on the numerical model of **Figure 1b**, simulated with EOF (P-NP-NS, symbols) and without EOF (P-NP, curves), for varying surface charge (σ). When (a) $c_{in} = c_{ex} = 3$ M and (b) $c_{in} = c_{ex} = 140$ mM, neglecting EOF is valid.

6. Flow ICR can induce NDR

6a. NDR is sensitive to nanopipette charge and radius

Extended simulations show that the NDR regime only arises for specific flow ICR conditions. In **Figure S19**, we replot the simulated pipette data in **Figure 6a** (blue curves) alongside simulated data with moderate changes to the nanopipette (red curves). When modifying the surface charge (**Figure S19**, left) or the radius (**Figure S19**, right), resistance still increases with voltage but no NDR regime is observed. We attribute the low yield of NDR pipettes to our inability to precisely control these parameters during fabrication.

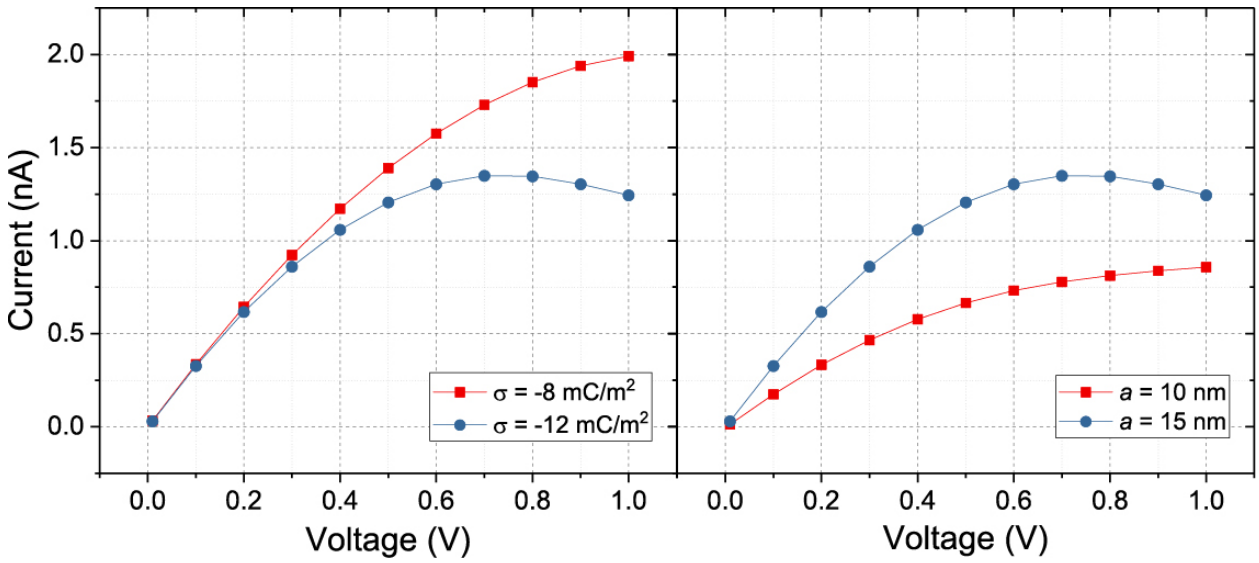

Figure S19. Simulated current-voltage relationships for the pipette in **Figure 6a** (blue curves), alongside a slightly modified pipette (red curves). Upon modifying the surface charge (left) or the radius (right), NDR is no longer observed.

6b. Radial concentration distributions enable vortex flows to induce NDR

We attribute the experimental NDR in **Figure 6a** to the vortex flow in **Figure 6b** (left) depleting intermediate pipette concentrations to below the values of the filling solutions (**Figure 6c**, black curve). Supporting this claim, we observe that net ion concentrations are enriched near the pipette wall, relative to the centerline. We demonstrate this effect in **Figure S20**, which displays radial ion concentrations for the cross-section of the pipette at z = 400 nm (traversing the NDR vortex of **Figure 6b**), when V = 1.0 V. Because the double layer enrichment of K^+ exceeds the depletion of Cl^-, net ion concentration is enriched near the pipette wall. The corresponding radial velocity gradient (**Figure 6b**, left) pumps ion-rich fluid from the pipette at a faster rate than nearby volumes of fluid. In order to ensure that the net ion flux through the vortex flow region is equal to the net flux upstream and downstream, the hydrostatic backflow fluid must deplete of ions. This explanation is analogous to the fluid continuity constraints that induce the vortices (**Figures 2a,b** and **S9**).

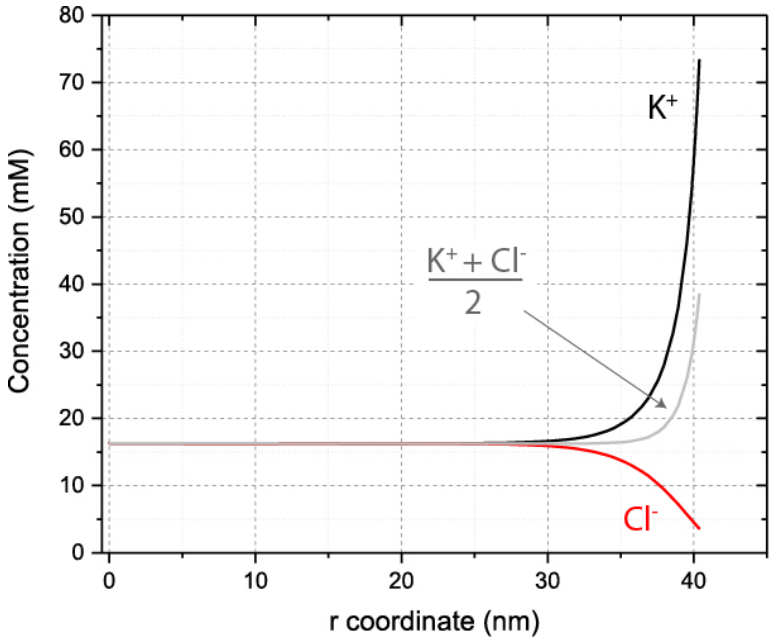

Figure S20. Simulated radial concentration profiles for the pipette in **Figure 6b** (left), at height z = 400 nm, where the net ion concentration is enriched near the wall. Combined with fast fluid flow near the wall and mass continuity constraints, the ion enrichment near the wall forces the hydrostatic back flows to deplete of ions.

6c. NDR coincides with concentration depletion below bulk solution levels

Ion concentrations across intermediate positive voltages are shown in **Figure S21** to depict the development of the V = 1.0 V concentration profile in **Figure 6c** (black curve). As voltage increases and vortices rotate faster, hydrostatic back flows increasingly deplete the concentration levels within the pipette, as evidenced by the curves approaching and ultimately crossing the dashed blue line around z = 500 nm. In simulation, the onset of NDR occurs when the intermediate concentration reduces below the value of the more dilute filling solution, as shown by the pink curve (V = 0.8 V) crossing the dashed blue line (c_{in} = 30 mM).

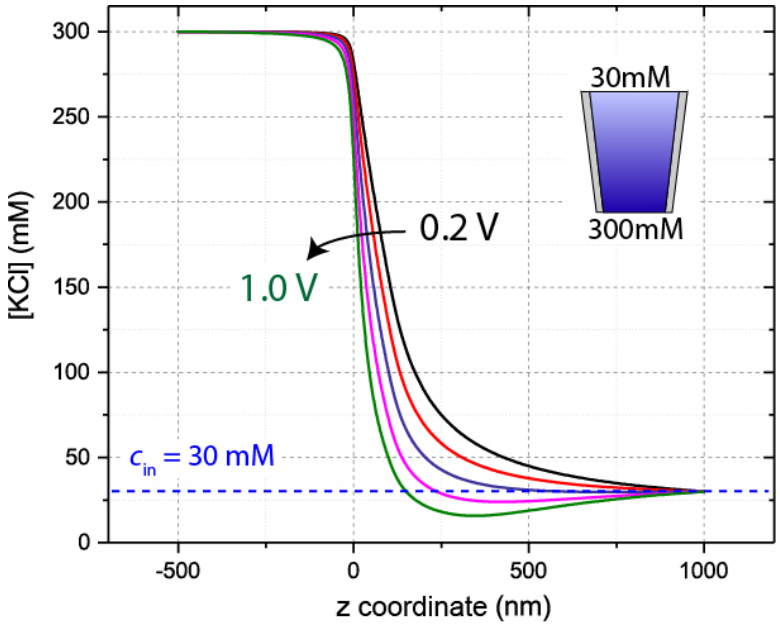

Figure S21. Simulated centerline concentrations for the pipette in **Figure 6a**, when $V > 0$ V. Concentration depletes as voltage increases, and NDR arises at the voltage ($V = 0.8$ V, pink curve) where the concentration inside the pipette ($z > 0$) depletes below the value of the more dilute filling solution ($c_{in} = 30$ mM, dashed blue line)

6d. Linear EOF is observed downstream from internal pipette vortices

EOF is linear downstream from vortex flows of **Figure 6b**, as shown in **Figure S22**, which depicts the truncated portions of the data in the former. Linear EOF prevails despite the nonuniform zeta potential distribution in the region (**Figure 7a**), which we attribute to the reduced voltage gradient at the tip (due to the smaller voltage drop that occurs across the more concentrated solution).

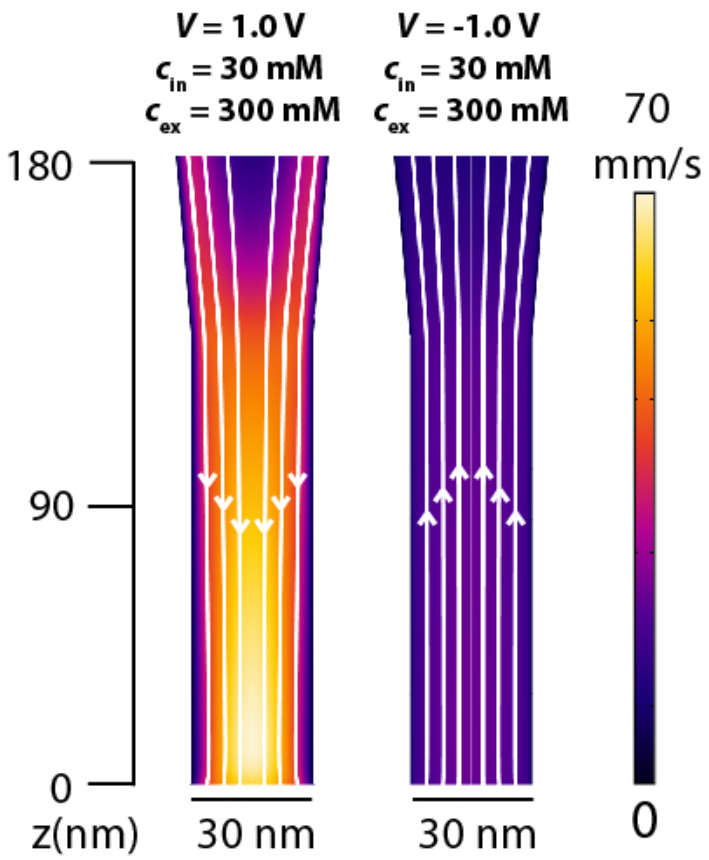

Figure S22. Simulated velocity heatmaps and streamlines for the pipette in **Figure 6a**, displaying the truncated portions of the data in **Figure 6b**. Linear EOF prevails through pipette tips, downstream from vortex flows of **Figure 6b.**

6e. Tunable ion selectivity is lost during NDR

For consistency, we simulate voltage-dependent ion transport selectivity for the pipette of **Figure 6a**. In **Figure S23**, when $c_{in} < c_{ex}$ and V is small, tunable permselectivity is maintained and inverts as compared to **Figure S16**. The observation is consistent with the mechanism described previously. However, anion selectivity is lost under these conditions, as an increasing preference for cation transport arises beyond V = 0.3 V and maintains through the NDR regime. The loss of anion selectivity is attributed to concentration depletion pushing the pipette further into the low-κa regime, such that transport becomes selective to counter-ions, as in Debye-overlap ICR (**Figure S16**, dotted curve).

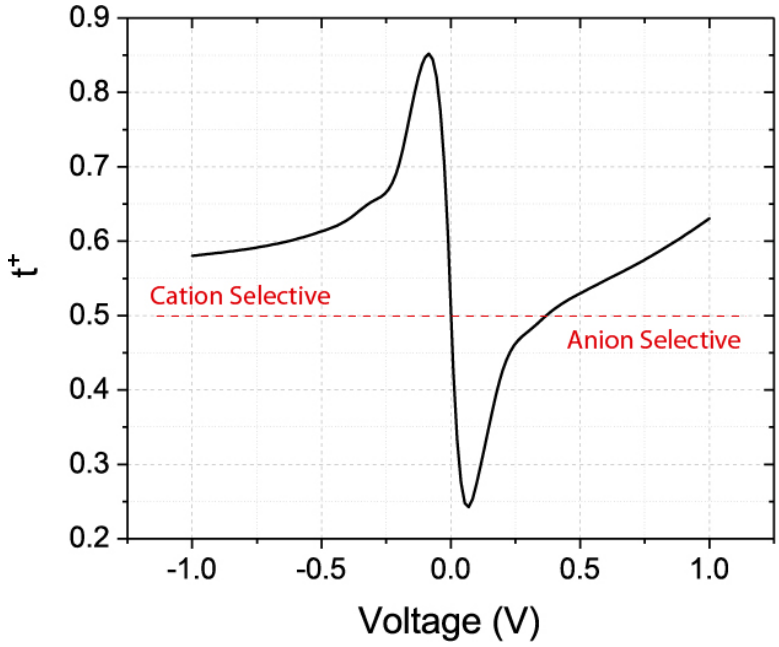

Figure S23. Simulated voltage-dependent transference (t^+) for the pipette of **Figure 6a**. When $c_{in} < c_{ex}$, ion selectivity is tunable, and voltage-dependent ion selectivity inverts as compared to when $c_{in} > c_{ex}$ (**Figure S16**, solid curve). Loss of selectivity beyond $V = 0.3$ V occurs as concentration depletion pushes the pipette further into the low-κa regime, drawing excess counter-ions into the electrolyte and resulting in selectivity for cations.

7. References

(1) Hamer, W. J.; Yung chi, Y. Osmotic Coefficients and Mean Activity Coefficients of Uni Univalent Electrolytes in Water at 25°C. *J. Phys. Chem. Ref. Data* **1972**, *1*, 1047–1100.

(2) Michael, H. N. Elementary Fluid Mechanics. *J. Franklin Inst.* **2003**, *244*, 495.

(3) Gregersen, M. M.; Andersen, M. B.; Soni, G.; Meinhart, C.; Bruus, H. Numerical Analysis of Finite Debye-Length Effects in Induced-Charge Electro-Osmosis. *Phys. Rev. E - Stat. Nonlinear, Soft Matter Phys.* **2009**, *79*, 066316.

(4) White, H. S.; Bund, A. Ion Current Rectification at Nanopores in Glass Membranes. *Langmuir* **2008**, *24*, 2212–2218.

(5) Sánchez, D.; Johnson, N.; Li, C.; Novak, P.; Rheinlaender, J.; Zhang, Y.; Anand, U.; Anand, P.; Gorelik, J.; Frolenkov, G. I.; et al. Noncontact Measurement of the Local Mechanical Properties of Living Cells Using Pressure Applied via a Pipette. *Biophys. J.* **2008**, *95*, 3017–3027.

(6) Sze, A.; Erickson, D.; Ren, L.; Li, D. Zeta-Potential Measurement Using the Smoluchowski Equation and the Slope of the Current-Time Relationship in Electroosmotic Flow. *J. Colloid Interface Sci.* **2003**, *261*, 402–410.

(7) Squires, T. M.; Bazant, M. Z. Induced-Charge Electro-Osmosis. *J. Fluid Mech.* **2004**, No. 509, 217–252.

(8) Lan, W. J.; Holden, D. A.; White, H. S. Pressure-Dependent Ion Current Rectification in

Conical-Shaped Glass Nanopores. *J. Am. Chem. Soc.* **2011**, *133*, 13300–13303.
(9) Luo, L.; Holden, D. A.; White, H. S. Negative Differential Electrolyte Resistance in a Solid-State Nanopore Resulting from Electroosmotic Flow Bistability. *ACS Nano* **2014**, *8*, 3023–3030.
(10) Wei, C.; Bard, A. J.; Feldberg, S. W. Current Rectification at Quartz Nanopipet Electrodes. *Anal. Chem.* **1997**, *69*, 4627–4633.
(11) Schoch, R. B.; Renaud, P. Ion Transport through Nanoslits Dominated by the Effective Surface Charge. *Appl. Phys. Lett.* **2005**, *86*, 253111.
(12) Smeets, R. M. M.; Keyser, U. F.; Krapf, D.; Wu, M. Y.; Dekker, N. H.; Dekker, C. Salt Dependence of Ion Transport and DMA Translocation through Solid-State Nanopores. *Nano Lett.* **2006**, *6*, 89–95.
(13) Yusko, E. C.; An, R.; Mayer, M. Electroosmotic Flow Can Generate Ion Current Rectification in Nano- and Micropores. *ACS Nano* **2010**, *4*, 477–487.
(14) Cao, L.; Guo, W.; Wang, Y.; Jiang, L. Concentration-Gradient-Dependent Ion Current Rectification in Charged Conical Nanopores. *Langmuir* **2012**, *28*, 2194–2199.
(15) Qiu, Y.; Lucas, R. A.; Siwy, Z. S. Viscosity and Conductivity Tunable Diode-like Behavior for Meso- and Micropores. *J. Phys. Chem. Lett.* **2017**, *8*, 3846–3852.
(16) Lan, W. J.; Edwards, M. A.; Luo, L.; Perera, R. T.; Wu, X.; Martin, C. R.; White, H. S. Voltage-Rectified Current and Fluid Flow in Conical Nanopores. *Acc. Chem. Res.* **2016**, *49*, 2605–2613.
(17) Schoch, R. B.; Han, J.; Renaud, P. Transport Phenomena in Nanofluidics. *Rev. Mod. Phys.* **2008**, *80*, 839–883.
(18) Yeh, L. H.; Hughes, C.; Zeng, Z.; Qian, S. Tuning Ion Transport and Selectivity by a Salt Gradient in a Charged Nanopore. *Anal. Chem.* **2014**, *86*, 2681–2686.
(19) Guan, W.; Fan, R.; Reed, M. A. Field-Effect Reconfigurable Nanofluidic Ionic Diodes. *Nat. Commun.* **2011**, *2*, 506–508.
(20) Tunuguntla, R. H.; Henley, R. Y.; Yao, Y. C.; Pham, T. A.; Wanunu, M.; Noy, A. Enhanced Water Permeability and Tunable Ion Selectivity in Subnanometer Carbon Nanotube Porins. *Science* **2017**, *357*, 792–796.